Available online at www.sciencedirect.com
SCIENCE DIRECT®
Journal of the European Ceramic Society 25 (2005) 3593–3604
www.elsevier.com/locate/jeurceramsoc

Optimization of $BaZrO_3$ sintering by control of the initial powder size distribution; a factorial design statistical analysis

B. Guillaume[a,*], F. Boschini[a], I. Garcia-Cano[a], A. Rulmont[a], R. Cloots[a], M. Ausloos[b]

[a] *Laboratoire de Chimie Inorganique Structurale, SUPRATECS, Department of Chemistry, Chemistry Inst. B6, University of Liège, Sart-Tilman, B-4000 Liège, Belgium*
[b] *Physique Statistique et des Matériaux, SUPRATECS, Department of Physics, Physics Inst. B5, University of Liège, Sart Tilman, B-4000 Liège, Belgium*

Received 6 May 2004; received in revised form 16 September 2004; accepted 18 September 2004
Available online 8 December 2004

Abstract

A factorial design statistical analysis has been conducted in order to obtain the optimum conditions in the solid state sintering process of barium zirconate bulk materials, optimum with respect to density, closed and open porosities. The optimized heat treatment permits to sinter a 99% dense barium zirconate sample at 1650 °C during only 2 h. When the temperature is higher than 1650 °C or when the heating time is longer than 2 h, a decrease in density is observed.

Keywords: Design of experiments (DOE); Grain growth; Sintering; Porosity; Perovskites; $BaZrO_3$

1. Introduction

Barium zirconate ($BaZrO_3$) is a well-known ceramics used in many electronic and refractory applications.

$BaZrO_3$ is characterized by a very high structural and thermal congruent melting point (≈2600/2700 °C),[1,2] a cubic perovskite structure with a lattice constant of 0.4193 nm [JCPDS 6-0399], a small thermal expansion coefficient, a poor thermal conductivity and an excellent mechanical and structural integrity under extreme thermal conditions.[3] Moreover, it has a very high stability under heating.

These physical properties make $BaZrO_3$ an ideal candidate for applications as crucibles when conducting reactions in presence of corrosive oxide melts, substrates for thin films deposition, and for thermal barrier coatings in aerospace industries.[4]

Barium zirconate is also known to be used as a functional ceramic with particular electrical properties. In suitable doped forms, alkaline-earth zirconate with perovskite structure become ionic and/or electronic conductors.[5–7]

In addition, barium zirconate is a potential material as humidity sensor.[8]

Zirconate compounds with high melting points, like $BaZrO_3$, are also present in fission products in nuclear industry. The knowledge of the behaviour of fission products and the properties of their compounds is very important for the safety and improvement of nuclear fuels. Some articles thus relate to the thermophysical properties of barium zirconate and other perovskite oxides like $BaCeO_3$ or $BaUO_3$.[2]

Note also that barium zirconate was reported to be a potential candidate material for interface engineering of alumina fibre/alumina matrix composites.[9]

Last but not least, $BaZrO_3$ can also play a significant role in the superconductivity research field. Since the discovery of high-T_c superconductivity in $REBa_2Cu_3O_7$ (RE: rare earth), much research is aimed at the synthesis of single crystals. At the beginning, the crystal growth of $REBa_2Cu_3O_7$ was achieved in Al_2O_3, SnO_2, Au, Pt, ThO_2, Y_2O_3, MgO or ZrO_2 crucibles.[1,10] Unfortunately, the crystal quality was

* Corresponding author. Tel.: +32 4 366 35 32; fax: +32 4 366 34 13.
E-mail address: b.guillaume@ulg.ac.be (B. Guillaume).

0955-2219/$ – see front matter © 2004 Elsevier Ltd. All rights reserved.
doi:10.1016/j.jeurceramsoc.2004.09.022

Table 1
Parameters and measured responses of the experimental design

Parameters	Abbreviation	Units	Variable kind	Explored range (−1 + 1)
Isotherm temperature	ISO	°C	Quantitative	1350–1650
Heating rate	HRT	°C/min	Quantitative	1–10
Heating time	HTM	min	Quantitative	120–720
Powder size (d_{50})	PWS	nm	Quantitative	600–1600

Responses	Abbreviation	Units	Experimental variance	Response range
Density	*D*	%	0.001–0.1	0–100
Open porosity	OP	%	0.005–0.2	0–100
Closed porosity	CP	%	0.001–0.5	0–100

poor—critical superconducting parameters like the London penetration depth (λ_1) or the electrical resistance at 77 K (R_S) were not acceptable for superconducting applications.[11] First $YBa_2Cu_3O_7$ growth was experimented in yttria-stabilized zirconia (YSZ) crucibles.

It has been observed that a $BaZrO_3$ layer is formed, which does not react with the $YBa_2Cu_3O_7$ flux.[1,12,13]

Some researchers are thus exploring the way of producing a commercial YSZ crucible covered by a protective $BaZrO_3$ layer. The main disadvantage of the $BaZrO_3$ ceramics stems in the high heating and long soak time necessary during sintering to achieve full density.[12,13] Moreover, $BaZrO_3$ is more expensive than YSZ. Whence, it seems that the use of a $BaZrO_3$ coating should be interesting for industrial manufacturing of non-corrosive crucibles.

The principal difficulty remains to producing a barium zirconate layer without any crack formation during processing.[14] Erb et al. preferred making $BaZrO_3$ crucibles in the bulk that, according to preliminary experiments, do not react with the corrosive melts. After Erb succeeded in synthesizing high quality $REBa_2Cu_3O_7$ single crystals by using a $BaZrO_3$ crucible,[1] many researchers developed $BaZrO_3$ crucibles for the synthesis of superconducting single crystals.[15–18] Up to now, only a few publications are available on the $BaZrO_3$ sintering process and control: Erb et al. suggested a heat treatment at 1700 °C during 48 h and obtained samples with 98.5% of the theoretical density.[1] Azad and Subramaniam[5] used a shorter heat treatment (dwell at 1600 °C during 6 h followed by heating at 1700 °C), but obtained materials with only 89% of the theoretical density. Moreover, they use sintering aids like Al_2O_3, MgO or Y_2O_3; these oxides contaminate the superconducting melt, and result in a higher viscosity which is not suitable for producing large single crystals.

Sin et al. reported a value of 95% of the theoretical density by using a heat treatment at 1500 °C during 10 h from a powder that was initially synthesized by the polyacrylamide method.[19] Dierickx et al. sintered a commercial powder at 1600 °C during 4 h and have measured a density around 97% of the theoretical density.[20]

In these reports, no explanation is given concerning the choice of the experimental parameters.

In this report, the sintering of $BaZrO_3$ dense material has been studied following a statistical analysis method. An orthogonal fractional factorial experimental design has been used to search for optimum, with respect to density, open and closed porosities, experimental parameters and to model the barium zirconate sintering process. There are in fact numerous advantages associated with the design of experiment through factorial design.[21] Factorial design allows estimating the effects of one parameter over a wide range of the other parameters, thus yielding conditions that are valid over a wide range of experimental situations.[22]

In this study, four sintering parameters were analysed simultaneously: [(i) the isotherm temperature; (ii) the heating rate; (iii) the heating time at isotherm temperature and (iv) the powder size (percentile $d_{50\%}$)]. Three responses have been measured: [(i) the density; (ii) the open porosity and (iii) the closed porosity] (Table 1). The main effects of each parameter, and the effects of interaction between parameters, were determined using the analysis of variance technique (ANOVA technique).

The selected design of experiments is thus composed of a "fractional factorial design" with star points located at the centre of faces of a cube (Fig. 1). This design allows the estimation of a quadratic model which is appropriate to model and optimize the sintering process. This fractional factorial design is unit variant and corresponds to a balanced and orthogonal arrangement of experiments. In others words, parameters are centred and scaled using the midrange, low and high values from the parameter definition (Table 1). This arrangement enables the effect of one parameter to be assessed independently of all the others. A more detailed treatment of factorial design can be found in specific literatures.[21,23] In the retained fractional factorial design, the number of design runs is 25 and two repetitions of the central point were done to estimate the experimental variance. A multiple linear regression (MLR)[24] was used to model responses. The results and fitting parameters are presented in the discussion part.

Based on this method, reliable results have been obtained. Thanks to the optimized heating treatment, barium zirconate samples with 99% of its theoretical density have been synthesized from commercial powder. Moreover, with the use of a statistical analysis method, we have put into evidence the influential sintering parameters. In so doing, it is possible to sinter dense samples or controlled porous samples according to the envisaged application.

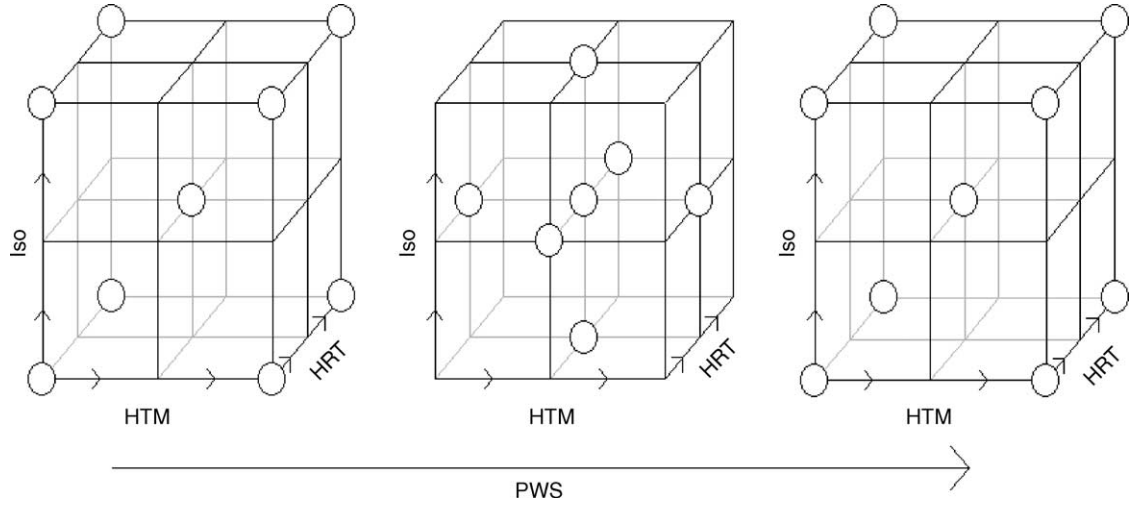

Fig. 1. Representation of the design region.

2. Experimental procedure

The $BaZrO_3$ (99% purity) powder was bought from Alfa-Aesar in June 2003. The powder purity was systematically checked by X-ray diffraction (XRD) analysis using monochromatic Cu Kα radiation (λ = 1.5406 Å), carried out on a X-ray diffractometer Siemens D5000.

2.1. Milling steps

Notice that, according to the design experiment worksheet presented in Table 2, we have to consider three different particle sizes. One thousand and six hundred nanometers is the mean size ($d_{50\%}$) of particles in the commercial powder. Granular size distributions were systematically checked by laser scattering measurements (wet measurements—Malvern Mastersizer granulometer) and are presented in Fig. 2. Mechanical grinding was carried out with a planetary grinder (Retsch PM 400\2) using tungsten carbide jar and alumina or zirconia's balls (diameter 10 and 3 mm, respectively). The powders were milled under the following conditions: wet milling, powder/balls/solvent weight under 1:2:1 proportions, respectively, a few dispersant drops—PMAA-NH_4 known as Darvan C.[25] The rotation speed of the jars was fixed at 200 rpm. Statistical analysis of the sintering process was conducted with a $BaZrO_3$ powder milled in water.

In a first set of experiment, we mill the powder with alumina balls. The particle size was reduced at approximately 40% of its initial size. After sintering (1650 °C/12 h), we observed that the relative density was reduced for the milled powder: only 83% of relative density compared to 93% for the un-milled powder. X-ray diffraction analyses performed on the sintered products after milling reveal the presence of a secondary phase identified as barium aluminium oxide—$BaAl_2O_4$, as shown in Fig. 3. In this figure, the up-

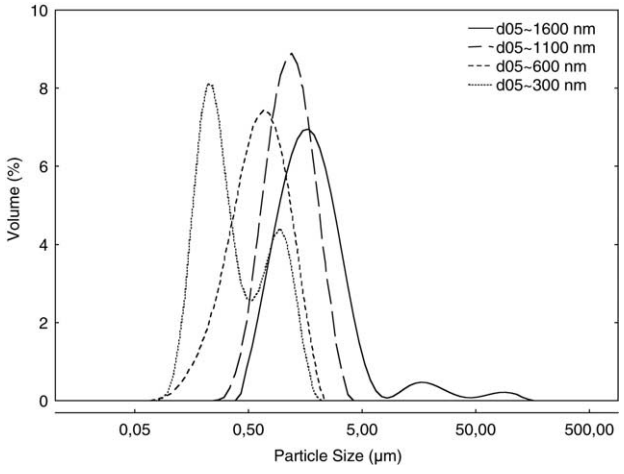

Fig. 2. Granular distribution of un-milled and milled powders.

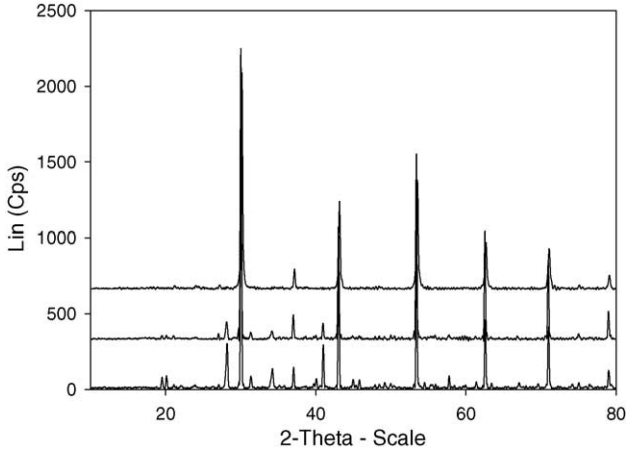

Fig. 3. Comparative X-rays diffractograms of samples which are sintered following the same heating conditions. Only the milling time was different (respectively, 0, 1 and 2 h for the upper, middle and lower diffractograms).

Table 2
Experimental worksheet and experimental results

Centred and scaled parameters				Responses		
ISO	HRT	HTM	PWS	*D*	OP	CP
−1	−1	−1	−1	69	30	1
1	−1	−1	−1	97	0	3
−1	1	−1	−1	82	17	1
1	1	−1	−1	99	0	1
−1	−1	1	−1	68	32	0
1	−1	1	−1	98	1	1
−1	1	1	−1	87.5	1	11.5
1	1	1	−1	94.5	2.5	3
−1	−1	−1	1	60.5	39	0.5
1	−1	−1	1	94.5	1	4.5
−1	1	−1	1	68	31	1
1	1	−1	1	92	0.5	7.5
−1	−1	1	1	75	24	1
1	−1	1	1	88	1.5	10.5
−1	1	1	1	75	23.5	1.5
1	1	1	1	94	1.5	4.5
−1	0	0	0	77.5	21	1.5
1	0	0	0	92.5	1	6.5
0	−1	0	0	93.5	0.5	6
0	1	0	0	93	1	6
0	0	−1	0	88.5	3.5	8
0	0	1	0	94	0.5	5.5
0	0	0	−1	97	0.5	2.5
0	0	0	1	89.5	1.5	9
0	0	0	0	92.5	1	6.5
0	0	0	0	92.5	1	6.5
0	0	0	0	92	1.5	7

per diffractogram corresponds to pure, un-milled $BaZrO_3$ sample. The median and lower diffractogramms reveal the presence of secondary phases like ZrO_2 and $BaAl_2O_4$. It is noticed that the presence of secondary phases seen in the X-ray diffractogram increases as a function of the milling time.

A chemical reaction between $BaZrO_3$ and Al_2O_3 was thus identified, as was previously reported.[26] A noticeable density decrease occurs when the barium aluminium oxide phase is present in the samples. This is understood taking into account the fact that $BaAl_2O_4$ theoretical density is only 4.08 g/cm^3 [JCPDS 82-2001] while $BaZrO_3$ density is 6.24 g/cm^3 [JCPDS 6-0399]. Energy dispersive X-ray (EDX) analysis performed on the same sample reveals the presence of $BaAl_2O_4$ phase (darker region), as shown in Fig. 4.

Afterwards, powders were milled with ZrO_2 balls (MgO stabilized). No trace of contamination was reported from EDX analyses. ZrO_2 balls have thus to be preferred in order to mill powders used for the statistical analysis study of the sintering process. Six hundred nanometers ($d_{50\%}$) is the size limit obtained by milling, with a quasi monomodal distribution. Upon attempting to reduce the particle size less than 600 nm ($d_{50\%}$), a bimodal distribution appears. Even if a bimodal distribution would be beneficial to improve compaction,[27,28] it is possible to observe grain segregation during the compaction step and of course a possible differential sintering mechanism accompanied by cracks' formation.[29,30] Consequently the third particle size selected has to be around 1100 nm ($d_{50\%}$). Granular size distributions for the three selected particle sizes are presented in Fig. 2 for completeness.

2.2. Sintering steps

The powders were isostatically pressed at 2250 bars (without any binder) into 10 mm diameter discs. The green pellets densities were calculated from the weight and dimensions of

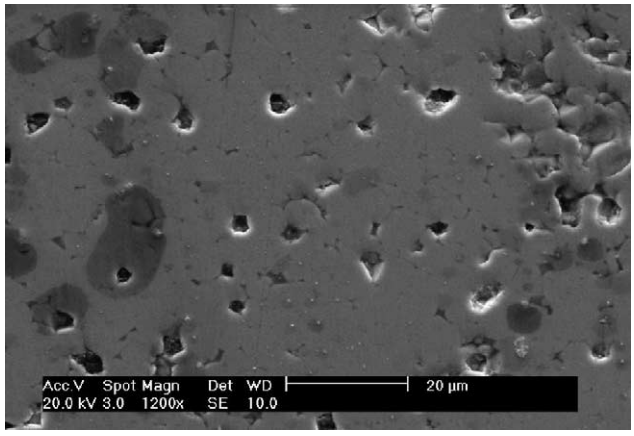

Fig. 4. Scanning electron micrograph of $BaZrO_3$ sample contaminated by $BaAl_2O_4$ secondary phases (darker phases).

the samples. The relative green densities were approximately equal to 55% of the theoretical density of $BaZrO_3$.

The samples were then sintered in air, according to the experiment worksheet described in the following.

Final densities, open and closed porosities were measured using the Archimede's method with 1-butanol as solvent. The sintered samples microstructures were observed by scanning electron microscopy (Philips ESEM XL30).

3. Experimental results and discussion

Based on the above fractional factorial design (Fig. 1), 27 experiments were conducted ($N = 27$). The resulting data are presented in Table 2.

Data have been fitted by using a multiple linear regression model[24] (MLR—Eq. (1)) with MODDE 6.0 software from UMETRICS AB.

MLR is based on finding the regression model which minimizes the residual sum of squares of the response variables.

Some steps are important for validating the multiple linear regression fitting:

(1) The first of them is the analysis of variance (ANOVA).[31] ANOVA is used to check regression model significance test and lack of fit test. In which case, ANOVA partitions the total variation (SS—sum of squares) of a selected response into a part due to the regression model and a part due to the residuals. At times, when replicated experiments are available, ANOVA also decomposes the residual variation into one part related to the model error and another part linked to the replicate error. Subsequently, the numerical sizes of these variance estimates are formally compared by means of *F*-tests.
   - ANOVA: regression model significance test; first decomposition.

     With least squares analysis, a mathematical model is created. It is possible to formulate a formal test to check if the model is good or not. In ANOVA, the first decomposition is $SS_{total} = SS_{regression} + SS_{residual}$ where the first member is the total variation in the response, corrected for the average. The amount of variation that we can model is given by the first term of second member and the amount of variation that we cannot model is given by the second term of the second member.

Usually, a model is considered as good if $SS_{regression}$ is high and if the unmodellable variation, $SS_{residual}$, is low. Mean squares (variance) are obtained by dividing the respective SS with the corresponding degrees of freedom (d.f.). The sizes of these two variances are compared by an *F*-test. This is accomplished by forming the ratio $MS_{regression}/MS_{residual}$ and then retrieving the probability *p* that these two variances originate from the same distribution. It is common practise to set $p = 0.05$ as the critical limit. On the sole condition that $p < 0.05$, the variance explained by the retained model ($MS_{regression}$) is significantly larger than the unexplained variance ($MS_{residual}$).

So, the first test assesses the significance of the regression model. All factors in the retained model are also characterized by a *p*-value. In this case, *p*-value is the probability to get the displayed value for the coefficient if its true value is zero. In others words, the 'null hypothesis' (H_0 hypothesis) is tested for each MLR equation factors (parameters and their interactions). For a determined factor, if H_0 hypothesis is verified, this factor is said to be not influent ($\beta = 0$, Table 3). In practice, a confidence level of 95% is considered, i.e. the alpha-level is set at 5%. The alpha level corresponds to the risk to reject H_0 hypothesis when this hypothesis is verified. The test of H_0 hypothesis is thus rejected and the factor is considered as influent when $p < 0.05$. From *p*-values reported for each MLR equation factors, parameters and interactions are considered to be influent or not. Moreover, for one given parameter, the smallest the *p*-value is, more influent is this parameter onto the model. The scaled and centred coefficients of model fitted are resumed in Table 3. This table shows that some parameters and/or interaction

Table 3
Scaled and centred coefficient of MLR model

	Eq. symbol	Coefficient SC	Standard error	*p*	Conf. Int (±)
Constant	α	92.3889	0.959006	<0.0001	2.033
ISO	β_1	10.4167	0.67812	<0.0001	1.43755
HRT	β_2	2.33334	0.67812	0.0033	1.43755
HTM	β_3	1.27778	0.67812	**0.0778** (!)	1.43755
PWS	β_4	−3.1111	0.67812	0.0003	1.43755
ISO × ISO	β_{11}	−8.41668	1.17454	<0.0001	2.48991
ISO × HRT	β_{12}	−2.40625	0.719255	0.0041	1.52475
ISO × HTM	β_{13}	−2.09375	0.719254	0.0102	1.52475
ISO × PWS	β_{14}	0.531249	0.719254	**0.4708 (!)**	1.52475
HRT × PWS	β_{24}	−1.21876	0.719254	**0.1095** (!)	1.52475
ISO × HRT × PWS	β_{124}	1.84375	0.719254	0.0208	1.52475
R.S.D.	ε	2.877			

Table 4
ANOVA table

	d.f.	SS	MS (variance)	*F*-test	*p*	S.D.
Total	27	206378	7643.63			
Constant	1	203320	203320			
Total corrected	26	3057.66	117.602			
ANOVA 1: regression model significance test						
Total corrected	26	3057.66	117.602			10.8445
Regression	10	2925.22	292.522	35.3406	< 0.0001	17.1033
Residual	16	132.436	8.27723			2.87702
ANOVA 2: lack of fit test						
Residual	16	132.436	8.27723			2.87702
Lack of fit	14	130.936	9.35255	12.4701	0.077	3.05819
Pure error	2	1.5	0.749999			0.866025

Fit result

N	d.f.	Q^2	R^2	Cond. No.	*Y*-miss
27	16	0.81	0.957	3.2255	0

are not influent ($p > 0.05$). Nevertheless in regard with the *p*-values, we can consider that parameter 'heating time' (HTM) and interaction HRT × PWS are relatively influent. Interaction ISO × PWS must be taken into account, because this interaction is essential to introduce a triple interaction ISO × HRT × PWS in the model, which is influent.

Notice that parameter HTM and interaction HRT × PWS become influent if the alpha level is set at 10%.

- ANOVA: lack of fit test; second decomposition.

The second test consists in comparing the model error and the replicate error. Actually, a second decomposition of sums of squares may be made: $SS_{residual} = SS_{model\ error} + SS_{replicate\ error}$. The unmodellable variation ($SS_{residual}$) has two components, one arising from the fact that the model is imperfect, the model error, and one arising from the fact that there is always variation when doing replicated experiments, the replicate error (experimental variance). In the ideal case, the model error and the replicate error are small and of similar size. Whether this is the case may be formally tested with an *F*-test in which one the two variances ratio ($MS_{model\ error}/MS_{replicate\ error}$) is *F*-tested. Whence, if the alpha-level is fixed at 5%, a *p*-value >0.05 ensures that the model has small model error and good fitting power. The model equation is said do not present a lack of fit.

From $SS_{residual}$ and $SS_{total\ corrected}$, it is possible to deduce the correlation coefficient R^2. This parameter is the classical quantity used to evaluate the goodness of fit.

The predicted variation parameter Q^2 is deduced from $SS_{predictive\ residual}$ and $SS_{total\ corrected}$. Q^2 estimates the predictive power of a model.

ANOVA table, its two tests and other fitting parameters are resumed in Table 4. In this one, 'Cond. No.' and '*Y*-miss' represent the condition number (an orthogonality measure of the design) and the number of missing response value, respectively.

(2) The second step to validate the model consists in analysing the residues distribution.

The raw residual is the difference between the observed and the fitted (predicted) value. Ideally, fit residues

Table 5
Comparison between values predicted (P) by the model and measured values (M)

ISO (°C)	HRT (°C/min)	HTM (min)	PWS (nm)		*D* (%)	Lower limit	Upper limit
1450	8	100	1100	P	87.6	84.9	90.2
				M	85		
1500	8	600	600	P	98.3	95.3	100
				M	96		
1625	4	300	1100	P	95.3	93.3	97.3
				M	96		
1400	3	180	1600	P	75.3	72.2	78.4
				M	74		
1568	10	120	600	P	99.5	95.8	103 (!)
				M	97		

Table 6
Summary table of grain growth experiment at very high temperature

ISO (°C)	HRT (°C/min)	HTM (min)	PWS (%)	*D* (%)	CP (%)	ESEM picture	Area distribution	Average area (μm^2)
1650	10	120	600	99	1	Fig. 7	Fig. 7b	10
1700	10	120	600	96	4	Fig. 8	Fig. 8b	25
1700	10	2880	600	95	5	Fig. 9	Fig. 9b	100

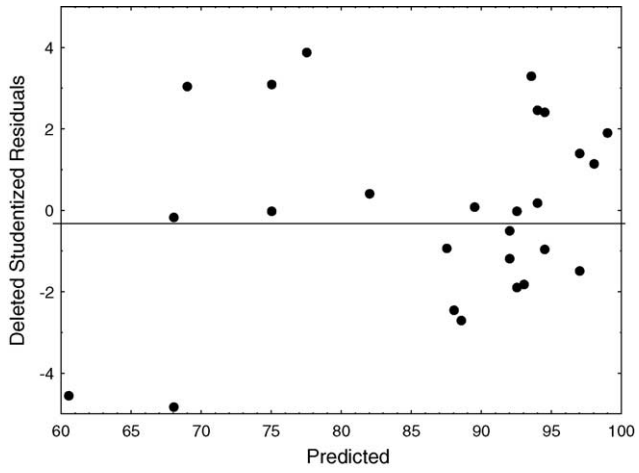

Fig. 5. Residuals plot vs. predicted values for density.

must be distributed randomly in all variable range and for all predicted responses. Therefore, it is important to estimate the residues distribution. Fig. 5 represents the residual plot versus predicted values for density model. It appears that residues are distributed randomly. The second condition to validate the model is fulfilled.

(3) As a last step to validate the model, let the predictions be verified. The verification of model prediction and model optimization are presented in Table 5. The prediction values of density are in agreement with the observed values, but they are located near the lower limit of predicted range. This could be explained by an un-perfect fit. It is important to precise that conclusions are valid for parameter values which are included in the defined initial range. Extrapolations out of this defined range are not statistically reliable.

Open and closed porosities responses are discussed in Appendix A because for the open porosity model, ANOVA lack of fit test reveals the presence of a lack of fit. For the closed porosity model, the overall fitting was not satisfactory.

Let's turn to the discussion part of the sintering process:

Fig. 6 represents the evolution of density as a function of the isotherm temperature and heating time. The heating rate and powder size are fixed at 10 °C/min and 600 nm, respectively. It is important to precise that this graph was plotted from the model and centred around the optimal point. Absolute values for one parameter are thus not very important, contrary to their evolution with respect to others parameters.

The most important information to extract from this graph is that heating time has beneficial effect at low isotherm temperature but have drastic effect at high isotherm temperature

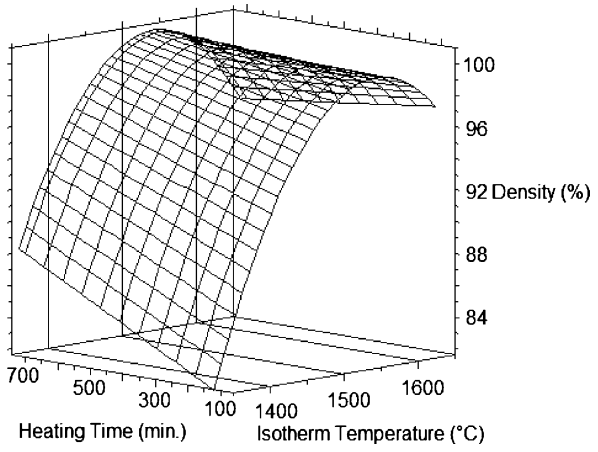

Fig. 6. Density as a function of heating time and isotherm temperature plot. Heating rate and powder size were fixed at 10 °C/min and 600 nm, respectively.

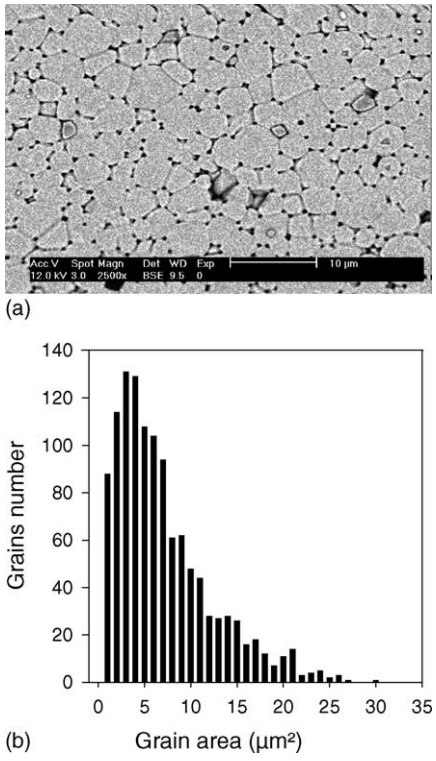

Fig. 7. (a) Scanning electron micrograph of $BaZrO_3$ sintered during 2 h at 1650 °C. (b) Grain area distribution plot for $BaZrO_3$ sintered during 2 h at 1650 °C, deduced from electron micrographs.

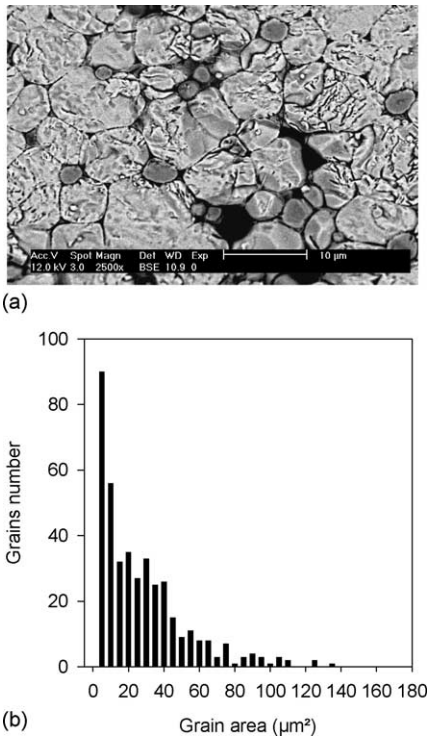

Fig. 8. (a) Scanning electron micrograph of $BaZrO_3$ sintered during 2 h at 1700 °C. (b) Grain area distribution plot for $BaZrO_3$ sintered during 2 h at 1700 °C, deduced from electron micrographs.

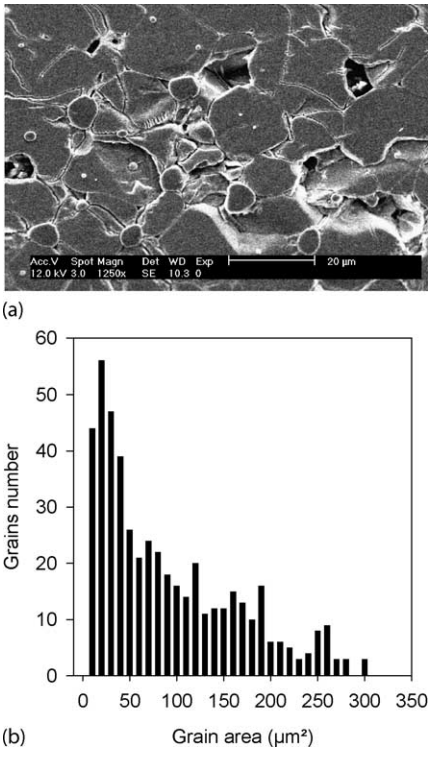

Fig. 9. (a) Scanning electron micrograph of $BaZrO_3$ sintered during 48 h at 1700 °C. (b) Grain area distribution plot for $BaZrO_3$ sintered during 48 h at 1700 °C, deduced from electron micrographs.

to get high density products. Indeed, the interaction ISO × HTM is negative ($\beta_{13} < 0$, Table 3).

To understand the density decrease when isotherm temperature is higher than an optimal temperature, the following explanation is given: it is known that there is a compromise between the grain growth and the densification mechanisms during heat treatment, especially during the final stage of sintering. If the sintering rate is too fast and/or if the isotherm temperature is too high, the grain growth mechanism is faster than the densification ones. To illustrate this phenomenon, the microstructures of three samples were studied by scanning electron microscopy and image analysis (Table 6). Samples were fixed in epoxy resin and then polished with silicon carbide grinding papers and diamond paste. Chemical etching was essential to reveal grains boundaries. Samples were soaked during 20 s in the etching solution (95 ml H_2O_2 (30 vol.%), 5 ml HCl (37%), 5 drops of HF) and then washed in ethanol.

From our microscopic observations (Figs. 7–9), it is clear (Fig. 7b) that grain growth affects the distribution of grain size. A broad range of values for grain area is reached when only temperature (Fig. 8b) and both temperature and heating time (Fig. 9b) are increased. The results are compared in Fig. 10, leading to the conclusion that an abnormal grain growth mechanism is effective for $BaZrO_3$.

Abnormal grain growth is generally associated with an increase in closed porosity explaining why a density decrease is observed in samples when the sintering temperature is higher than 1650 °C, and/or the heating time is longer than 2 h. Such behaviour is confirmed by the microstructure reported in Figs. 8–10, where large pores are visible for samples heat-treated above 1650 °C. According to the hypothesis that atoms located at the grain boundary have a higher energy than those in the bulk (the grain boundary is characterized by a surface energy, often denoted γ_{gb}, typically on the order of 0.2–1 J/m^2), the driving force for grain growth is the decrease in free energy that accompanies reduction in the total grain boundary area.[32]

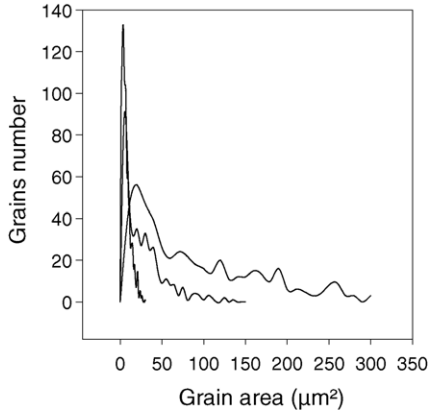

Fig. 10. Comparative plot of grain size distribution for $BaZrO_3$ sintered at 1650 °C for 2 h, 1700 °C for 2 h and 1700 °C for 48 h.

At high sintering temperatures, the sintered density decreases due to swelling from trapped gases in the pores. The gas-filled pores coalesce and grow due to grain growth.[33]

4. Conclusions

With only 27 experiments, lot of information are related by a statistical analysis. For example:

- We observe a strong dependence of isotherm temperature, an inverse relation between particle sizes and the so-obtained densities.
- It is easy to observe that if sintering is conducted from a relatively small particle size it is possible to achieve a good density preferentially if the heating rate is fast. Indeed, the superficial diffusion is then the predominant mechanism to give a porous material.
- It is equally possible to observe that there is a so-called saturation phenomenon as a function of the maximum isotherm temperature; in other words, the model detects an optimum temperature after which the density decreases.
- It is easy to predict at which temperature open porosity disappears for a given grain size powder and/or to a given heating rate and/or to a given soak-time.
- It is so easy to evaluate the maximum density attainable for a given temperature or for a given particle size.

Thus, the main results from this research can be summarized as follows: a fractional design statistical analysis was conducted to optimize the sintering of barium zirconate materials. It is reported that the milling step, depending on the nature of the milling medium, can produce degradation of the material by reaction leading to a decrease in density when particle size has been reduced.

An optimized heat treatment was deduced from the linear regression model extracted. It is concluded that a 99% dense $BaZrO_3$ bulk material can be formed at 1650 °C during 2 h. Increasing further the isotherm temperature or the heating time leads to a decrease in density due to abnormal grain growth associated with the formation of trapped porosity.

Acknowledgements

This work is financially supported by the Belgium French Community (Communauté Française de Belgique) within the framework of a Concerted Research Action on Granular Materials no 02/07-293. Great thanks to Jonathan Noël, for precious advice on the statistical analysis part.

Appendix A. Closed and open porosities as a function of the experimental parameters selected

Values of open and closed porosities are reported as a function of density in Fig. 11 as scatter plots.

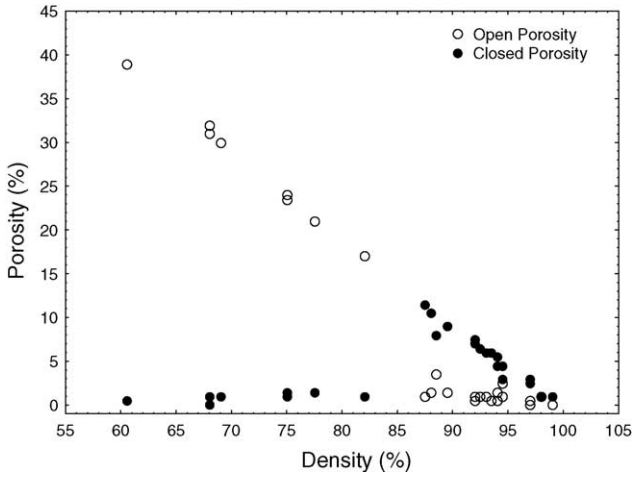

Fig. 11. Scatter plot reporting open and closed porosity as a function of density.

It appears a difference of porosity behaviour. Actually, open porosity as well as closed porosity are characterized by two different behaviours. As seen in Fig. 11, for a density lower than a critical value (around 85%), open porosity decreases linearly with density. For the density above this critical value, the closed porosity is inversely proportional to the density. It is possible to make this discrimination on the basis of isotherm temperature. In the range where the isotherm temperature is 1350 °C, the open porosity decreases linearly with density. As for the closed porosity, a linear decay is observed in the range 1500–1650 °C. Correlation coefficients (R) have thus been calculated and are presented in Table 7.

These differences in porosity behaviour as a function of isotherm temperature can explain why a lack of fit is present in the initial open porosity model. Indeed, the open porosity behaviour as a function of density is strongly dependent on the isotherm temperature range.

So, with a few caution, it is possible to model the porosity (open or closed) from the density model. As shown in Fig. 12, the density and porosity present an inversely proportional relationship (correlation coefficient, R (D, $OP_{[1350]}$, $CP_{[1500–1650]}$) = −0.99934), the type of porosity depending on the considered isotherm temperature range.

Let's turn to a new way for presenting the data based on a principal components analysis. In brief, the idea is that the principal components will provide a new set of (uncorrelated) variables defined as linear combination of the original ones. One of the objective of principal components is then to reduce the dimension of the system corresponding to the

Table 7
Correlation coefficient table

Isotherm range (°C)	Correlation coefficients		
	R (D, OP)	R (D, CP)	R (OP, CP)
1350–1650	−0.9893	0.4721	−0.5959
1350	−0.9979	0.4027	−0.4614
1500–1650	−0.6448	−0.9887	0.5230

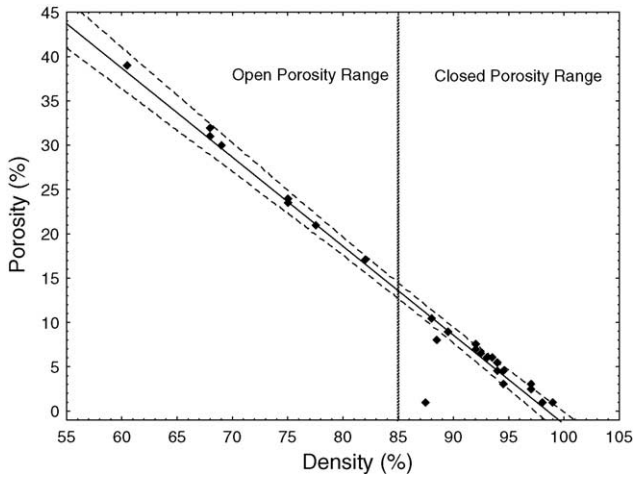

Fig. 12. Linear representation of the inversely proportional relationship between density and porosity.

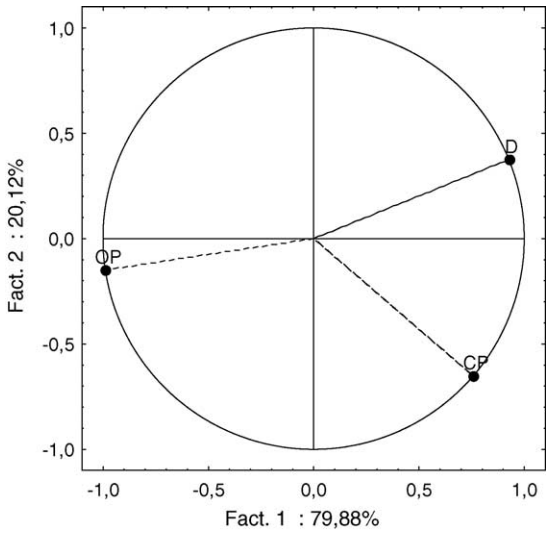

Fig. 13. Correlations of the two new principal components with the original variable (DOE responses).

original variable, and then to provide pictures in lower dimensional spaces. Geometrically, variables are thus represented in a new system of coordinates which are defined as "artificial variables".

Notice that the reduction of variable number (in this case, three to two) is not synonymous of information loss. Indeed, first and second new variables explain, respectively, 79.88 and 20.12% of the total information. The use of 2D graphs is then useful to explain a phenomenon with three degrees of freedom. This technique allows reducing the variable number giving interpretable geometric representations which make easy correlations between factors and responses.

Fig. 13 represents the three original variables (DOE responses) in the new system of coordinates given by the principal components analysis.

Fig. 14 corresponds to clusters of individuals (DOE experiments) in the two principal components coordinates system. The legend associated at each point represents the centred and scaled DOE factors. Corresponding density value has also been indicated for remarkable points.

The main message from the two graphs is summarized as follows: the first component is mainly characterized by an opposition between open porosity (OP) and closed porosity (CP)/density (*D*). In terms of individuals, the points on the left are more than anything representative of low isotherm temperature ($-1xxx$). Points relating to moderate and high isotherm temperature, respectively, ($0xxx$) and ($1xxx$), are localised on the right part of the graph. This confirms the hypothesis of the porosity double behaviour as a function of

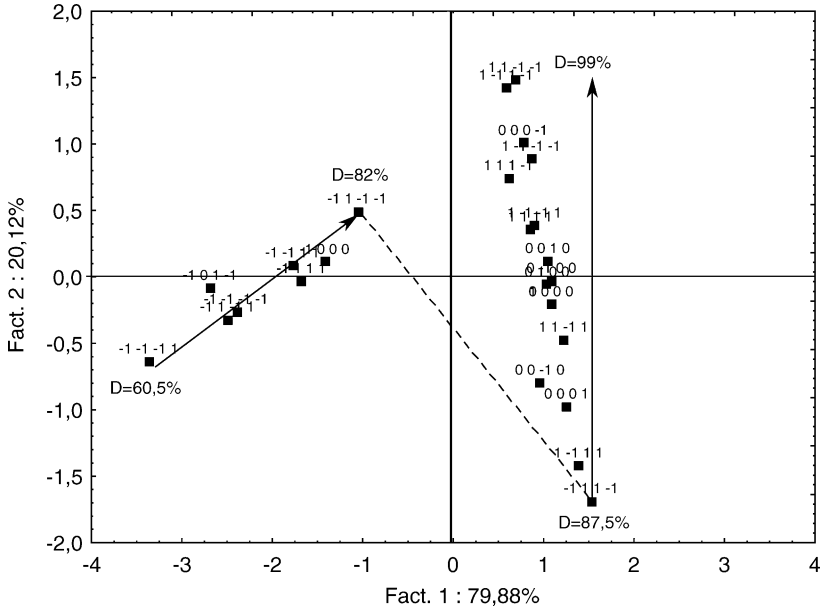

Fig. 14. Clusters of individuals (DOE experiments) in the two new principal components coordinates system.

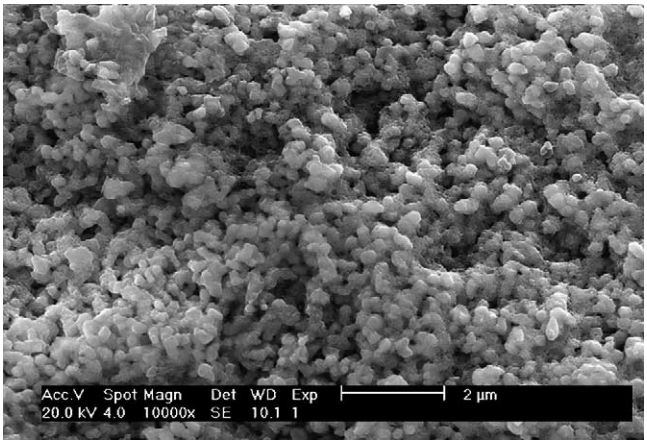

Fig. 15. Scanning electron micrograph of $BaZrO_3$ sample identified as (*D*, OP, CP) = (60.5, 39, 0.5)%.

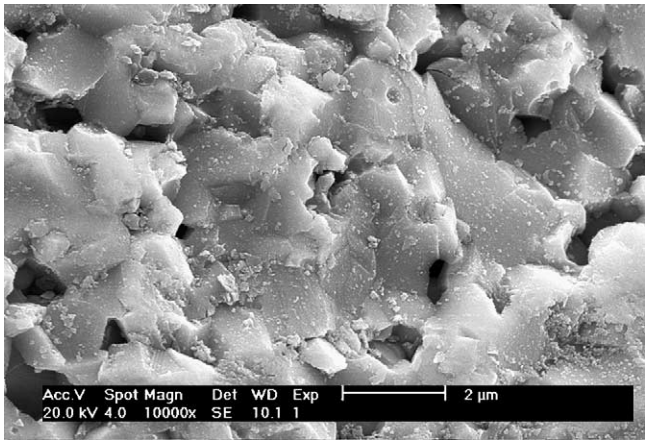

Fig. 17. Scanning electron micrograph of $BaZrO_3$ sample identified as (D, OP, CP) = (87.5, 1, 11.5)%.

the isotherm temperature. The second axis (second component) shows an opposition between closed porosity (CP) and density (*D*). With Figs. 13 and 14, it is thus also possible to deduce a relationship between the evolution of porosity type and the evolution of density.

The scatter plot analysis and the principal component analysis ensure to leave in obvious that at low density, the open porosity is dominant; an open porosity decrease is observed when the density increases. The open porosity becomes then negligible and closed porosity is then dominant. Afterwards, closed porosity linearly decreases with increasing density. Notice that the evolution of porosity type can be also illustrated with scanning electron micrographs. It is seen that the open porosity is predominantly present in the 60.5% and 82% samples (respectively Figs. 15 and 16). On the other hand, the porosity of the 87.5% sample is predominantly closed while residual open porosity can still be observed (Fig. 17). Of course, the 99% sample does not present any porosity (Fig. 18).

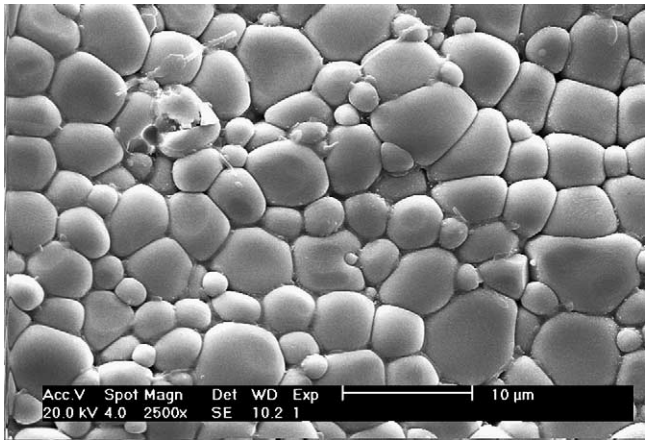

Fig. 18. Scanning electron micrograph of $BaZrO_3$ sample identified as (*D*, OP, CP) = (99, 0, 1)%.

$$Y = \alpha + \sum_{i=1}^{k} \beta_i X_i + \sum_{i=1}^{k} \beta_{ii} X_i^2 + \sum_{i=1}^{k} \sum_{j=i+1}^{k} \beta_{ij} X_i X_j + \varepsilon \quad (1)$$

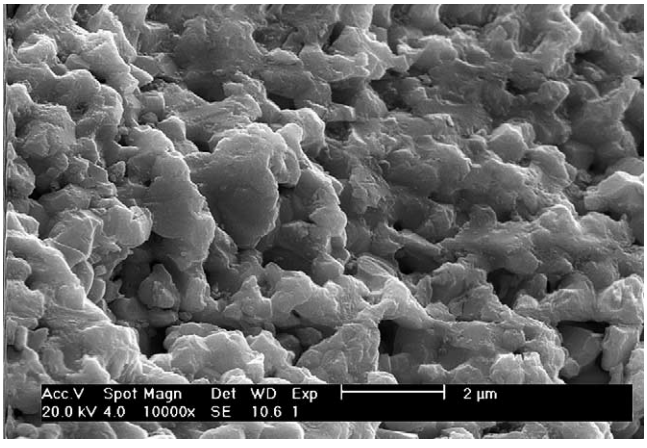

Fig. 16. Scanning electron micrograph of $BaZrO_3$ sample identified as (*D*, OP, CP) = (82, 17, 1)%.

References

1. Erb, A., Walker, E. and Flükiger, R., *Physica C*, 1995, **245**, 245–251.
2. Yamanaka, S., Hamaguchi, T., Oyama, T., Matsuda, T., Kobayashi, S-i. and Ken Kurosaki, K., *J. Alloys Compd.*, 2003, **359**, 1–4.
3. Azad, A. M., Subramaniam, S. and Teng Wan Dung, T. W., *J. Alloys Compd.*, 2002, **334**, 118–130.
4. Vassen, R., Cao, X., Tietz, F., Basu, D. and Stöver, D., *J. Am. Ceram. Soc.*, 2000, **83**(8), 2023–2028.
5. Azad, A-M. and Subramaniam, S., *Mater. Res. Bull.*, 2002, **37**, 11–21.
6. Haile, S. M., *Mater. Today*, 2003, **6**(3), 24–29.
7. Katahira, K., Kohchi, Y., Shimura, T. and Iwahara, H., *Solid State Ionics*, 2000, **138**, 91–98.
8. Viviani, M., Buscaglia, M. T., Buscaglia, V., Leoni, M. and Nanni, P., *J. Eur. Ceram. Soc.*, 2001, **21**, 1981–1984.

9. Chen, Z., Duncan, S., Chawla, K. K., Koopman, M. and Janowski, G. M., *Mater. Charact.*, 2002, **48**, 305–314.
10. Gerhold, S., Aigner, M. and Assmus, W., *Physica C*, 1997, **282–287**, 719–720.
11. Srikanth, H., Willemsen, B. A., Jacobs, T., Sridhar, S., Erb, A., Walker, E. *et al.*, *Phys. Rev. B*, 1997, **55**(22), 14733–14736.
12. Alford, N. M c N., Templeton, A. and Penn, S. J., *Supercond. Sci. Technol.*, 1998, **11**, 703.
13. Schmidt, J. C., Tigges, A. and Schmitz, G. J., *Mater. Sci. Eng. B*, 1998, **53**, 115–118.
14. Robertz, B., Rulmont, A., Gilbert, B., Cloots, R., Ausloos, M. and Leroy, N., *Mater. Lett.*, 1999, **41**, 273–277.
15. Morita, Y., Motohashi, T., Sugihara, S. and Yamauchi, H., *Physica C*, 2002, **378–381**, 360–363.
16. Erb, A., Walker, E. and Flükiger, R., *Physica C*, 1996, **258**, 9–20.
17. Liang, R., Bonn, D. A. and Hardy, W. N., *Physica C*, 1998, **304**, 105–111.
18. Grammatika, N., McLachlan, D. S. and Sonnenberg, N., *Supercond. Sci. Technol.*, 1993, **6**, 469–475.
19. Sin, A., Montaser, B. E. and Odier, P., *J. Am. Ceram. Soc.*, 2002, **85**(8), 1928–1932.
20. Dierickx, D., Houben, I., Lapin, J., Delannay, F. and Van der Biest, O., *J. Mater. Sci. Lett.*, 1996, **15**, 1573–1576.
21. Lundstedt, T., Seifert, E., Abramo, L., Thelin, B., Nyström, Å., Pettersen, J. *et al.*, *Chemometr. Int. Lab. Syst.*, 1998, **42**, 3–40.
22. Loh, N. H. and German, R. M., *J. Mater. Process. Technol.*, 1996, **59**, 278–284.
23. Montgomery, D. C., *Design and Analysis of Experiments* (*3rd ed.*). Wiley, New York, 1991.
24. Draper, N. R. and Smith, H., *Applied Regression Analysis* (*2nd ed.*). Wiley, New York.
25. Jean, J-H. and Wang, H.-R., *J. Am. Ceram. Soc.*, 1998, **81**(6), 1589–1599.
26. Chen, Z., Duncan, S., Chawla, K. K., Koopman, M. and Janowski, G. M., *Mater. Charact.*, 2002, **48**, 305–314.
27. Onoda, G. Y., *J. Am. Ceram. Soc.*, 1983, **66**(4), 297–301.
28. Liniger, E. and Raj, R., *J. Am. Ceram. Soc.*, 1987, **70**(11), 843– 852.
29. Coble, R. L. and Ellis, J. S., *J. Am. Ceram. Soc.*, 1963, **56**(9), 461–466.
30. Ma, J. and Lim, L. C., *J. Eur. Ceram. Soc.*, 2002, **22**, 2197– 2208.
31. Eriksson, L., Johansson, E., Kettaneh-Wold, N., Wikström, C. and Wold, S., *Design of Experiments Principles and Applications*. Umetrics Academy/Learnways, Stockholm, 2000.
32. Rahaman, M. N., *Ceramic Processing and Sintering* (*2nd ed.*). Marcel Dekker Inc., New York.
33. German, R. M., *Sintering Theory and Practice*. Wiley, New York.